Our motivation is to investigate the low-density high strength steel by modifying the FeMnAlSiC high entropy steel and a novel $Fe_{36}Mn_{21}Cr_{18}Ni_{15}Al_{10}$ HEA reported in the literature [60, 149]. The majority of elements used here are of low cost (Fe, Mn, Al, Si, Cr, Ni, and C) and it gives rise to density lower than that of the conventional steel. In this present work, a non- equiatomic FeMnNiCrAlSiC high entropy steel was synthesized by the powder metallurgy route followed by SPS. Further attempts were made to study the mechanical properties i.e., microhardness, elastic modulus and compressive strength, and surface properties i.e., wear and biocompatibility of the SPSed sample.

4.1 Melting point prediction of the $Fe_{40}Mn_{14}Cr_{10}Ni_{10}Al_{15}Si_{10}C_1$ HES

The prediction of the melting point of the alloy through the various approaches are the machine learning (ML) approach, rule of mixture, and CALPHAD modelling, and the details of the calculation are given in subsection 2.8. The value of the melting point of the alloy was found to be 1400 ℃ (1673 K), 1402 ℃ (1675 K), and 1267 ℃ (1540 K) for the ML approach, rule of mixture, and CALPHAD, respectively. It was perceived that the melting point prediction of the HEAS by binary liquidous temperature concept was more precise as compared to other methods [229].

4.2 Alloying behaviour and structural analysis of milled powder sample

4.2.1 Phase evolution during mechanical alloying of the alloy

The X-ray diffraction (XRD) patterns of HES2 powder samples at different milling hours is shown in Figure 4.1(a). XRD pattern of starting mixing powder (pre-mixed) shows the diffraction peak of all corresponding elements. With increase in milling time, the intensities of individual element diffraction peaks decrease (Figure 4.1(a)). The diffraction peaks corresponding to C (graphite) and low-intensity peaks of Si (d~1.63(311), d~1.109(422)), Mn (d~1.63(521), d~1.216(721), Al (d~1.216(311)), Ni (d~1.216(220)) were not seen after 5 hours of milling. It was found that the elemental peaks started diminishing first, other than that of Fe and Cr. The diffraction peaks of Al vanished first as compared to other elements. After 20 hours of milling the diffraction peaks corresponding to Cr also vanished. Further increase in milling time up to 20 hours, most of the elemental peaks lost their identity except Mn and Ni. As the milling time increased to 30 hours, the peak intensities Mn and Ni were diminished. The majority of elemental peaks vanished except Si; it led to the formation of a dual-phase structure i.e., BCC (host lattice close to Fe) and χ-type phase (close to gamma brass) with a trace amount of Si in less than 30 hours of milling. However, after the formation of a solid solution phase within 30 hours of milling, the milling was continued for up to 40 hours to investigate the further effect of milling on the alloy. However, it showed no change in the phase except the minor change in the phase fraction of both the phases and decreased amount of Si. The increase in milling time up to 40 hours helped to form a more homogenized solid solution of fine grains with no significant grain refinement. Figure 4.1(b) shows the phase evolution in the (110) plane with the milling time. It is clearly seen in Figure 4.2(a), that the formation of a BCC (a = 0.286 nm) and χ-type phase (close to gamma brass structure) (a = 0.893 nm) structure with a trace amount of Si occurred in less than 40 hours of milling.

During milling, high lattice strain, and refined crystallite size are responsible for peak broadening and decrease in intensity all through the XRD (shown in Figure 4.1(a)). The crystallite size was decreased with the milling time but after a certain time, it saturated. Similarly, the lattice strain increased initially and then reached saturation. The variation of crystallite size and lattice strain with time is shown in Table 4.1. The crystallite size (CS) and lattice strain produced by milling were calculated by Rietveld refinement using the GSAS-II software. The Rietveld refinement analysis also confirmed the formation of BCC and χ-type phase 40 hours for BCC,

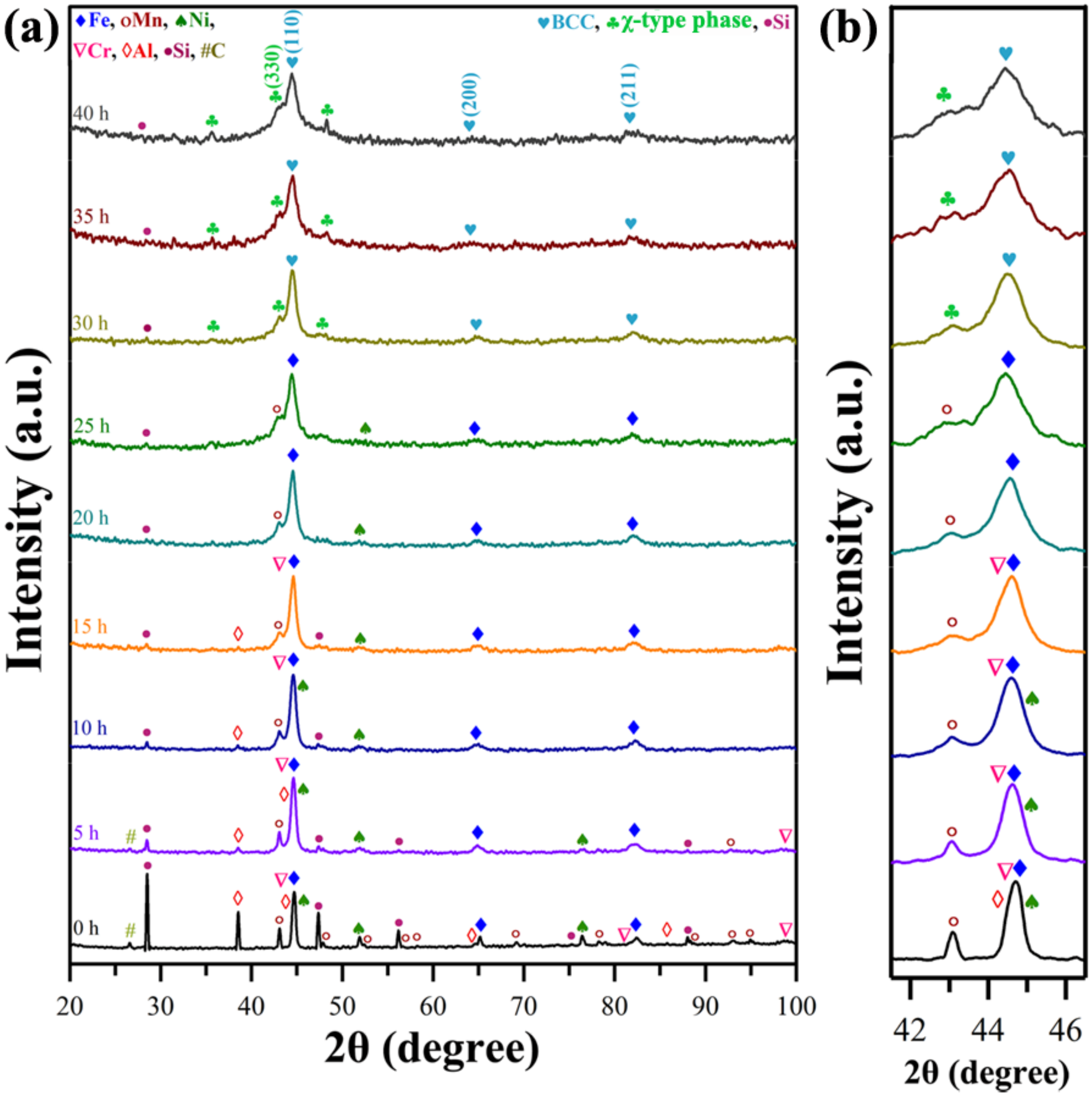

Figure 4.1: (a) XRD patterns of the milled samples at various milling time; (b) Enlarged view along the (110) plane in 2θ = 42º- 46º. This shows the alloying behaviour of alloy with the function of milling time, and it forms the dual-phase structure (BCC and χ-type phase) under 40 hours of milling.

χ-type phase, and Si, respectively. The reduction in crystallite size is due to mechanical milling. During milling, strain hardening and fracturing of particles (powder) occurred. There is not much notable refinement in the crystallite size, as the milling time increased from 30 to 40 hours. During the mechanical alloying process, the fracturing of powder particles and the introduction of elements in the host lattice of the high entropy alloy also increased the lattice strain.

Table 4.1: Variation in phase fraction, lattice strain, crystallite size and dislocation density with the milling time of the powder sample of HES2.

S.No.	Sample Designation	Phases	Phase Fraction (%)	Lattice Parameter (nm)	Crystallite Size (nm)	Lattice strain	Dislocation Density (m^{-2})
1	30 hr	BCC	78.0	0.286	16	1.21	2.29×10^{18}
		χ-type phase	18.0	0.893	13	1.04	7.78×10^{17}
		Si	3.0	0.543	32	0.98	----
2	35 hr	BCC	72.0	0.286	15	1.46	2.95×10^{18}
		χ-type phase	25.0	0.893	11	1.33	1.18×10^{18}
		Si	3.0	0.543	28	1.16	----
3	40 hr	BCC	68.7	0.286	12	1.60	4.04×10^{18}
		χ-type phase	29.8	0.893	8	1.71	2.14×10^{18}
		Si	1.5	0.543	23	1.31	----

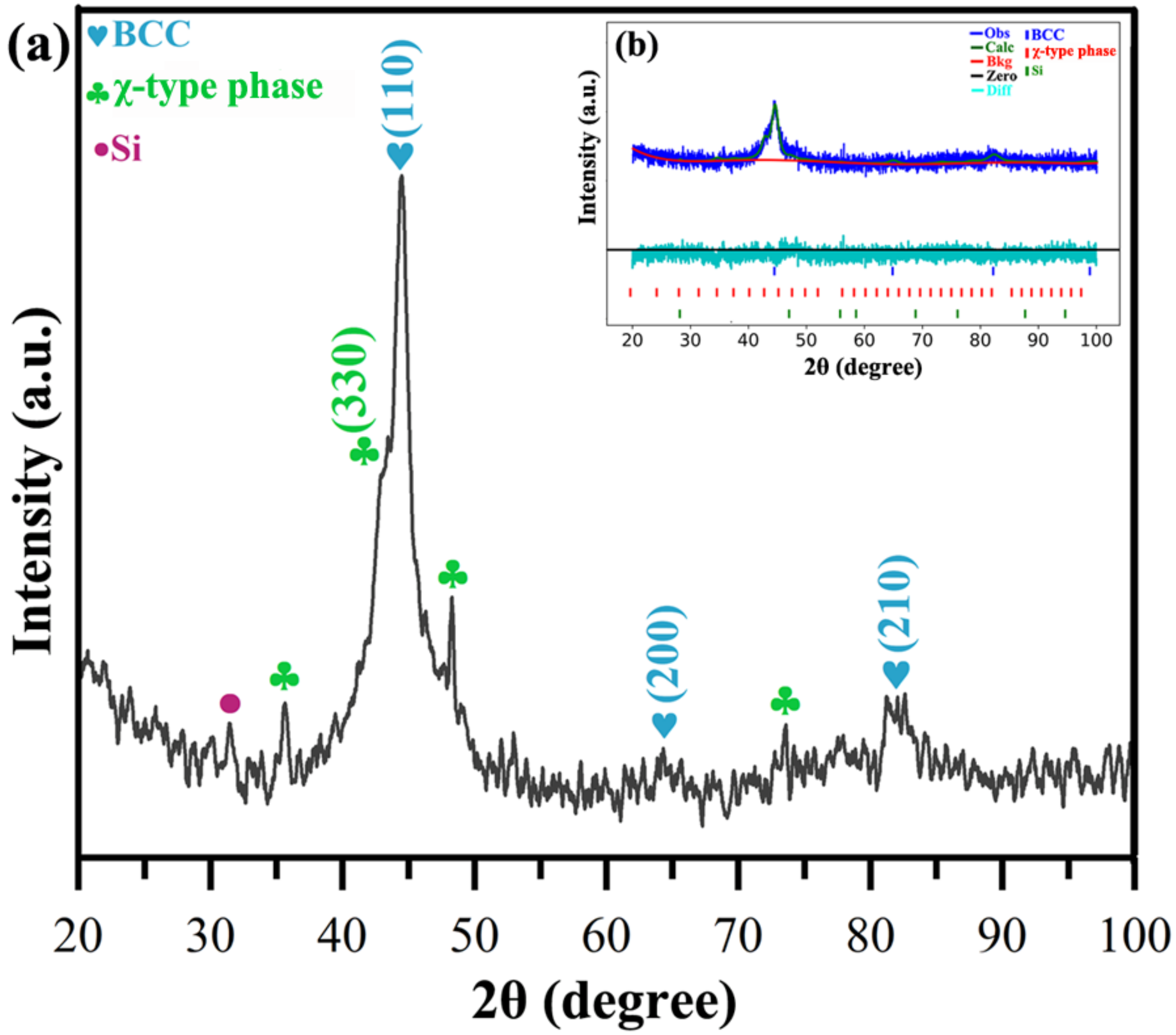

Figure 4.2: (a) XRD pattern of the 40 h milled powder sample; (b) Rietveld refinement of the corresponding sample. This represents the phase formed are dual-phase structure consisting of BCC and χ-type phase structure along with undissolved Si.

4.2.2 TEM analysis of milled powder sample

Figure 4.3(a, b, and c) illustrates the bright field, corresponding SAED pattern, and the dark field image of the 40 hours milled powder sample, respectively. The bright-field image shows the deformation of powder particles occurred due to the MA up to 40 hours. The selected area diffraction pattern (Figure 4.3(b)) shows the presence of χ-type phase structure. The diffraction spots correspond to the (211), (002), (321), and (420) reflection of the χ-type phase along $[1\bar{2}0]$

zone axis. Figure 4.3(c) shows the dark field image gathered from the (002) plane, which shows the nanocrystalline nature of the 40 hours milled powder sample.

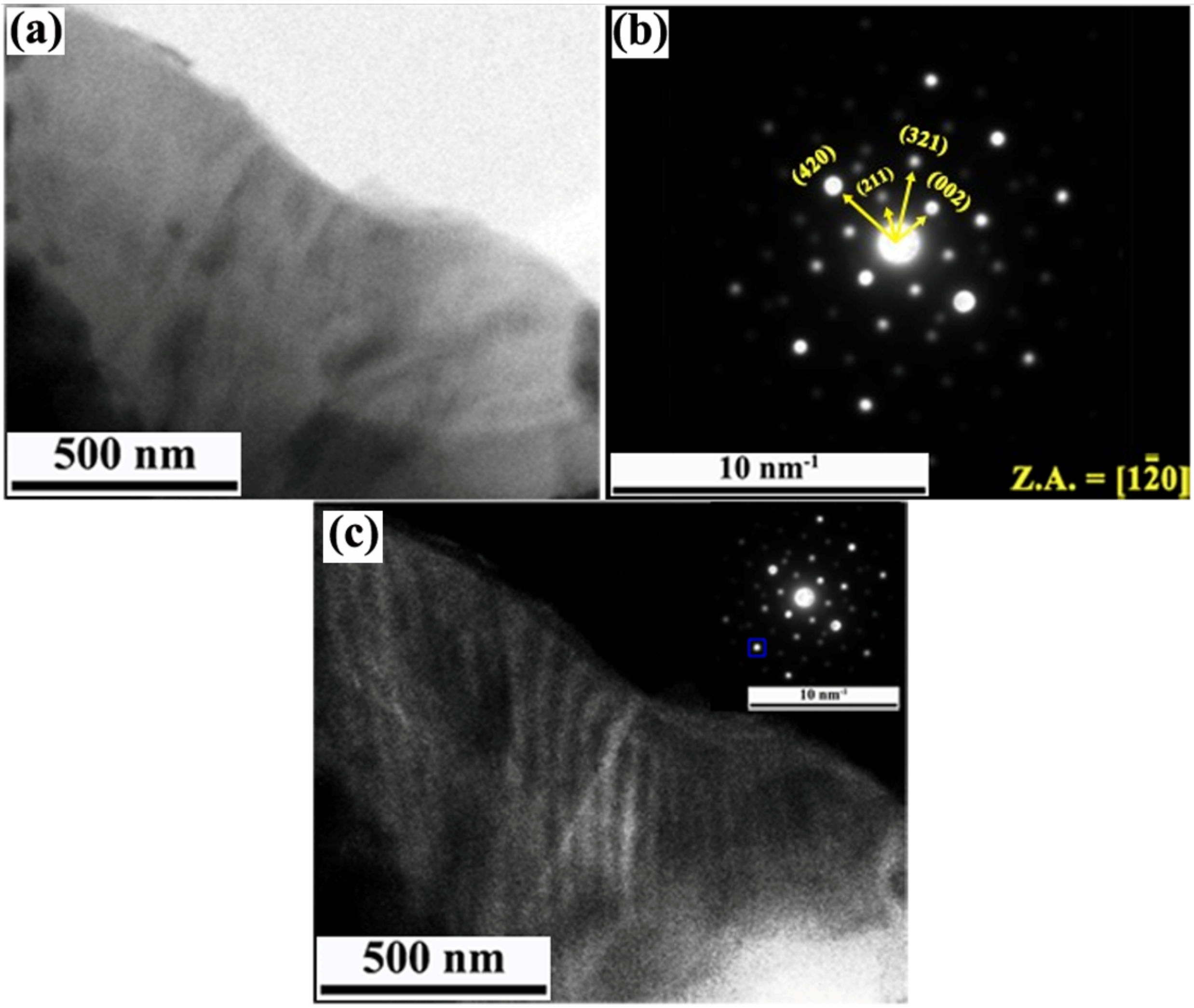

Figure 4.3: (a) TEM bright-field image of the 40 h milled powder sample; (b) its corresponding selected area diffraction ring pattern; (c) dark field image of the 40 h milled powder sample. SAED pattern corresponds to the χ-type phase structure.

The formation of nanostructured grains with a size of less than 15 nm was observed in the dark-field image (Figure 4.3(c)). This result was also ascertained from the Rietveld refinement of the XRD data of the powder samples, which is listed in Table 4.1.

4.2.3 Powder morphology and chemical analysis of milled powder sample

Figure 4.4(a-d) shows the SEM micrograph of the HES2 at different milling times i.e., 10, 20, 30, and 40 hours, respectively. The SEM micrographs at 40 hours milling time and full area EDS spectrum of 40 hours milled powder are shown in Figure 4.4(e). The morphological features of milled powder as a sizeable river pattern on the surfaces can be discerned. This type of morphological features may be attributed to repeated fracture and continuous deformation during milling.

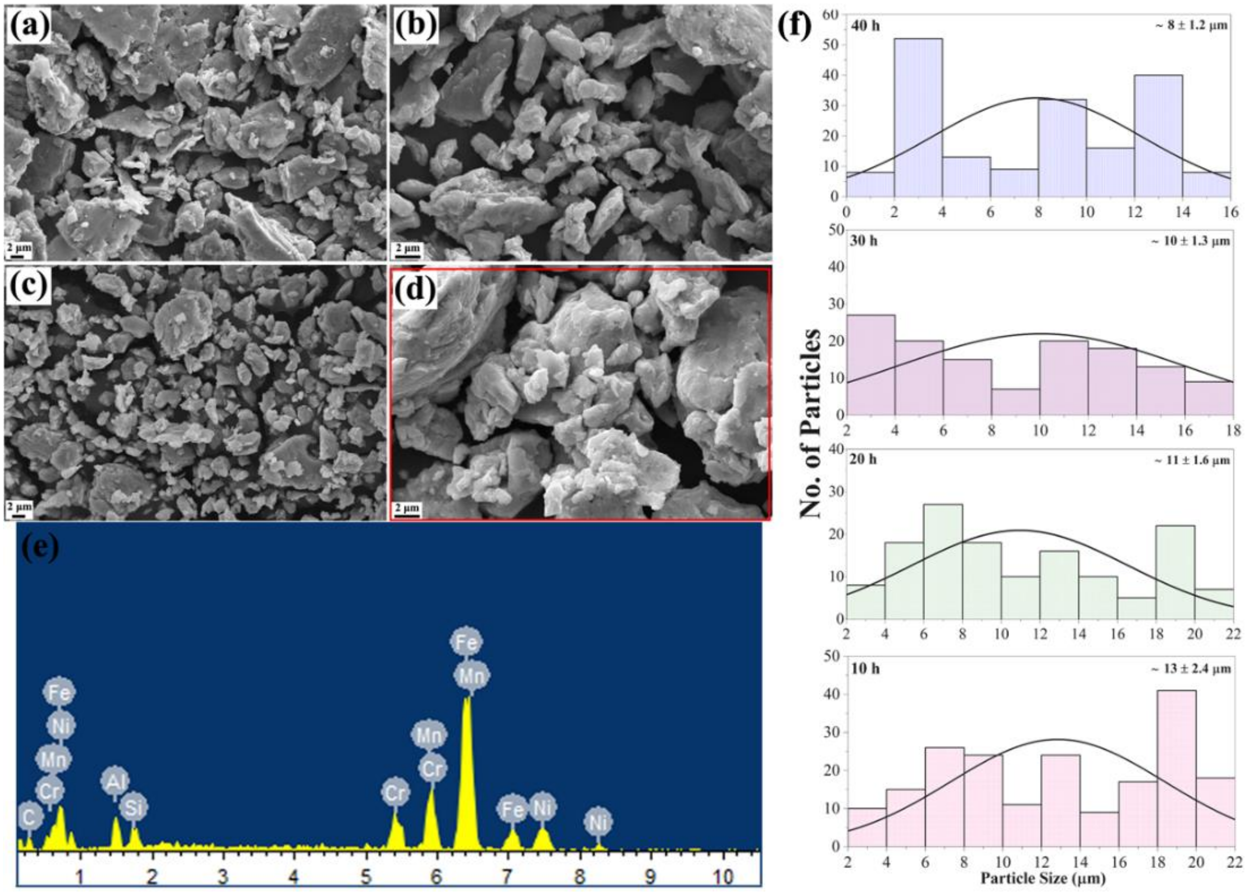

Figure 4.4: (a-d) SEM micrographs of powder samples milled at different milling time i.e., 10 h, 20 h, 30 h and 40 h, respectively. Figure 4.4(d) also marked the full area for EDS analysis; (e) Full area EDS analysis of 40 h milled powder; (f) Histograms showing the distribution of the particle size of milled samples from top to bottom for 40 h, 30 h, 20 h and 10 h. The histogram shows the distribution of the powder particle with the milling time. The average powder particle decreases with the prolongs milling time.

The average particle size of HES2 powder particles after 40 hours of milling is approximately between 7-10 µm. Figure 4.4(f) shows the particle size distribution (histogram) of milled powder. It was observed that the milled powder was of different sizes and shapes, varying from 1-22 µm. The average particle size decreased with the milling time and the values were found to be ~ 13 ± 2.4 µm, 11 ± 1.6 µm, 10 ± 1.3 µm, and 8 ± 1.2 µm for 10, 20, 30, and 40 hours, respectively. The particle size was measured using ImageJ software. Figure 4.5 shows the microstructure of the 40 hours green pellet and its corresponding mapping and the point EDS analysis. Table 4.2 lists the elemental composition of 40 hours milled powder from different areas i.e., full area, spot 1, and spot 2.

Table 4.2: The EDS analysis at different location i.e., full area and point EDS for the 40 h milled sample of HES2.

Elemental composition (at%)							
Sample condition	**Scan area**	**Fe**	**Mn**	**Ni**	**Cr**	**Si**	**Al**
40 hours milled sample	**Full area**	42.0	14.10	9.50	10.20	9.10	14.20
	Spot 1	45.10	14.30	10.32	9.80	7.24	13.14
	Spot 2	51.70	18.60	5.51	21.0	1.19	2.0

The marked point one is rich in Fe and the presence of all other elements is distributed evenly and it corresponds to BCC (ferritic phase) structure. The marked point two is rich in Fe, Cr, and Mn and lean in Al, Si, and Ni, and their stoichiometry is very close to the χ-type phase structure. The EDS mapping of the 40 hours green powder pellet also confirms the dual-phase structure i.e., the χ-type phase structure is rich in Fe, Cr, and Mn, and lean in Ni, Al, Si, and C. The unsymmetrical area marked (Figure 4.5) from the blue line shows that the Al, Si, and C elements are lean in χ-type phase structure and this area is rich in Fe, Mn, and Cr.

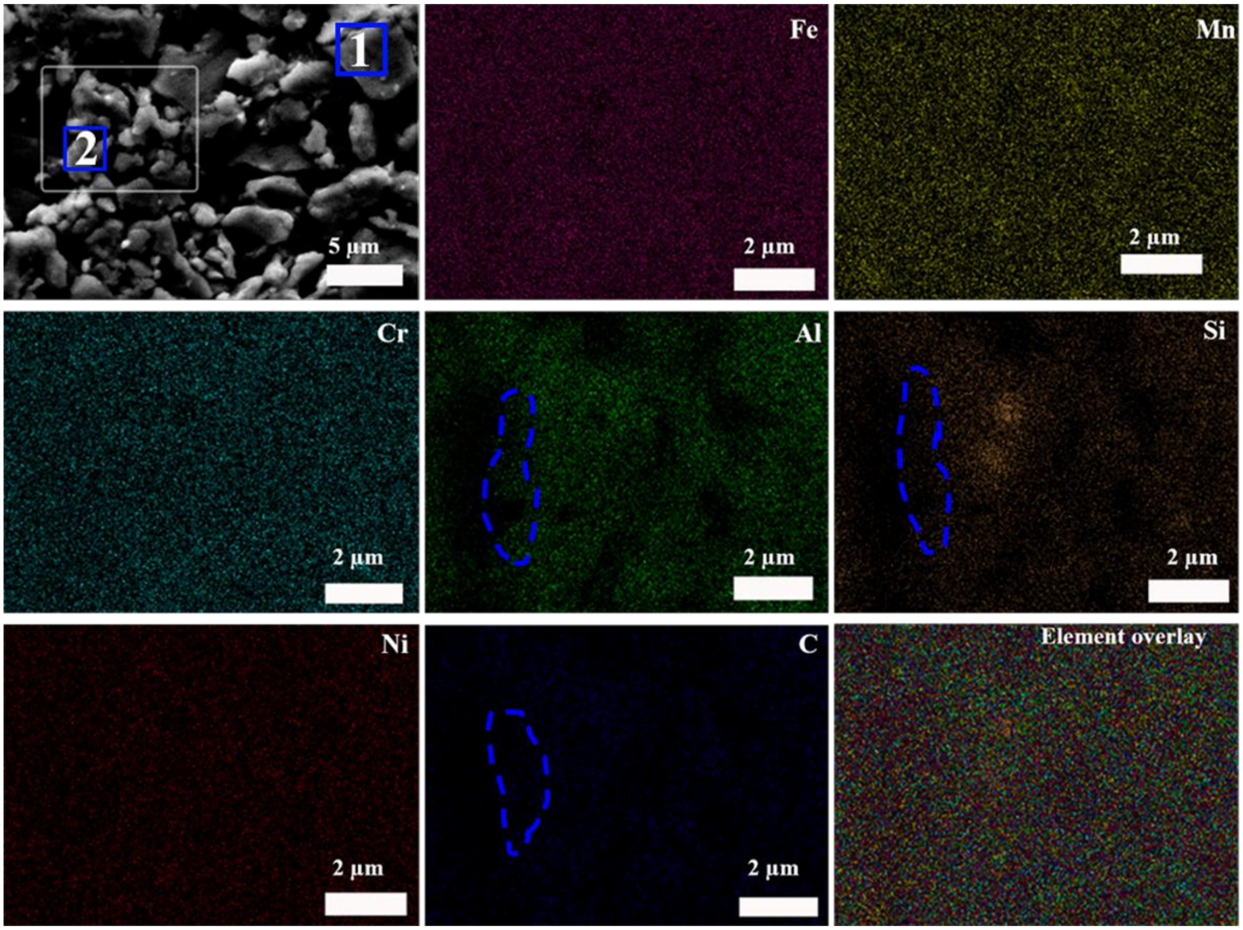

Figure 4.5: SEM micrograph of the 40 h milled powder, marked for point EDS analysis and EDS mapping. This shows the area elemental mapping and the elemental overlay. This clearly illustrates that the χ-type phase structure is rich in Fe, Cr and Mn. The unsymmetrical area marked from dotted blue line shows that the Al, Si and C elements is lean in χ-type phase structure.

4.3 Thermal stability and phase evolution of milled powder sample

High-temperature microstructural stability of HES2 is critical as this alloy are also designed to operate at high temperatures. Therefore, DSC and ex-situ XRD tests have been conducted. Figure 4.6 illustrates the DSC curve of the 40 hours milled powder sample, which reveals various exothermic events at 460 °C (733 K) and 650°C (923 K). To substantiate the phase transformation of 40 h milled powder, ex-situ XRD pattern (Figure 4.7(a)) at various temperatures, namely, 25 °C, 400 °C, 600 °C, 700 °C and 900 °C were obtained. This analysis reveals that there is a phase transformation occurring in the structure at around 500 °C. The DSC and ex-situ XRD confirm that the 40 hours milled powder is thermally stable up to 400 °C, as ex-situ XRD does not show any new peak evolution (shown in Figure 4.7(a)) and DSC curve (shown in Figure 4.6) also does not show any exothermic peak. The ex-situ XRD at 600 °C annealed powder shows the new peak evolved which is correlated with the Cr_3Si (cP8). This

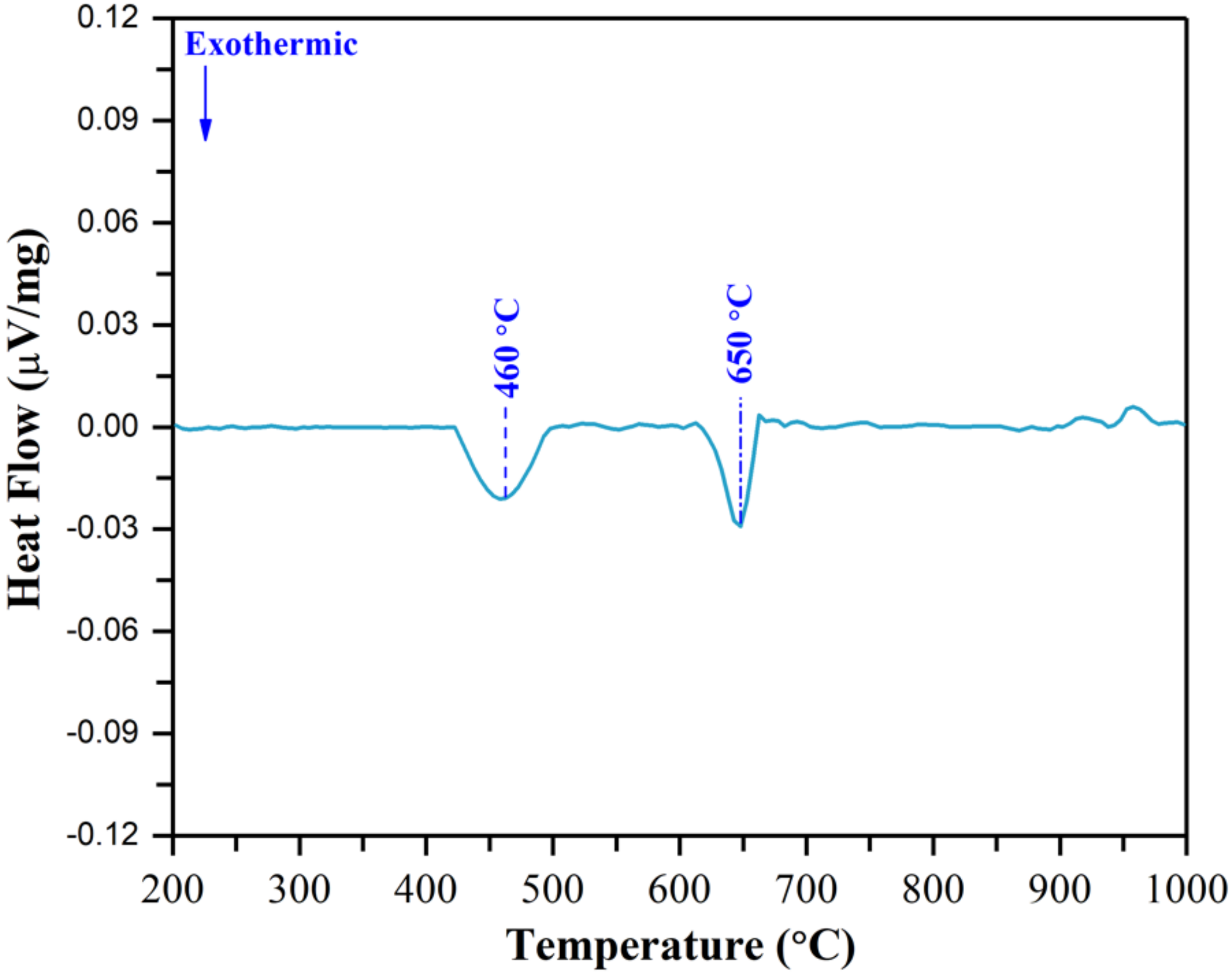

Figure 4.6: DSC thermogram of the 40 h milled powder of the non-equiatomic FeMnNiCrAlSiC high entropy steel from 200 °C to 1000 °C.

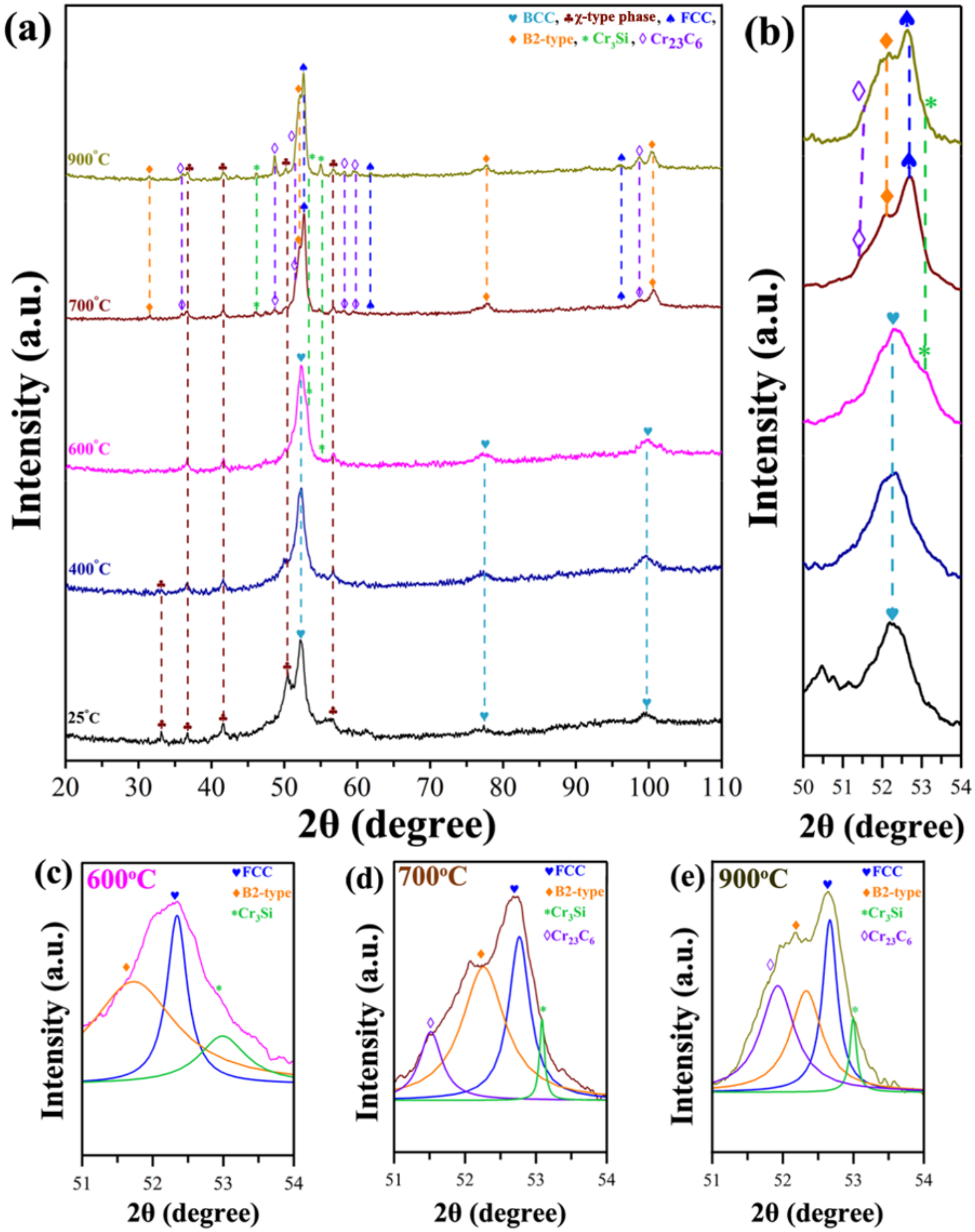

Figure 4.7: (a) Ex-situ XRD diffraction pattern of the milled sample at 25 °C, 400 °C, 600 °C, 700 °C and 900 °C; (b) Enlarge view of diffraction peaks along the (110) plane in 2θ = 50º-54º; (c-e) Deconvoluted peaks for the 600 °C, 700 °C and 900 °C, respectively. The formation of Cr_3Si-type intermetallic phase is correlate with exothermic event at 460 °C.

confirms that the exothermic peak is at 460 °C. Further, ex-situ XRD at 700 °C, shows the evolution of new diffraction peaks, which corresponds to the formation of FCC solid solution and $Cr_{23}C_6$ type, and ordering of BCC phase. This confirms the exothermic heating events at 650 °C. The enlarged view of the annealed sample in the 2θ range of 50º - 54º is shown in Figure 4.7(b). The deconvolution of phases around (110) peak of BCC phase for samples annealed 600 °C, 700 °C, and 900 °C are presented in Figure 4.7(c, d, and e), respectively. Afterwards, no phase change occurred but the amount of the FCC phase was increased. The Rietveld refinement of the annealed sample was done using GSAS-II software and it was listed in Table 4.3. This table listed the phase fraction, lattice parameter, crystallite size, and lattice strain of the various phases formed at 400 °C, 600 °C, 700 °C, and 900 °C.

4.4 Structural and microstructural analysis of SPSed sample

Figure 4.8(a), shows the XRD pattern of the HES2 after spark plasma sintering (SPS) at 1000 °C (1273 K). The SPSed sample of non-equiatomic FeMnNiCrAlSiC high entropy steel mainly consists of dual-phases: FCC phase (γ- austenitic), B2-type (Ni-Al type) along with Cr_3Si and $Cr_{23}C_6$ type intermetallics. The deconvoluted image in the 2θ range of 51º-54º is displayed in Figure 4.8(b). The final milled powder alloy consisting of two BCC structures transformed after SPS into a more stable FCC solid solution that coexisted with silicide and carbide. The Rietveld refinement of the SPSed sample was done and this also ascertained that the dual-phase structure consisting of FCC and B2-type along with silicide and carbide formed, which is illustrated in Figure 4.8(c).

Figure 4.9(a and b) show the SEM (Back Scattered Electron) micrographs of the sintered sample of non-equiatomic FeMnNiCrAlSiC high entropy steel at different magnifications. In the

Table 4.3: The phase fraction, lattice parameter, crystallite size and lattice strain of the annealed sample at 400 °C, 600 °C, 700 °C, 900 °C and SPSed samples of the HES2.

Condition	**Phases**	**Phase fraction (%)**	**Lattice parameter (nm)**	**Crystallite size (nm)**	**Lattice strain (%)**
400 °C; GoF = 1.05, χ^2 = 1.10	BCC	78.70	0.286	27	0.81
	χ-type phase	21.30	0.893	25	0.76
600 °C; GoF = 1.04, χ^2 = 1.07	BCC	75.70	0.286	36	0.74
	χ-type phase	11.30	0.893	32	0.61
	Cr_3Si	13.00	0.455	28	---
700 °C; GoF = 1.23, χ^2 = 1.80	FCC	48.70	0.362	52	0.66
	B2	32.00	0.290	49	0.47
	$Cr_{23}C_6$	8.00	1.066	30	---
	Cr_3Si	6.00	0.455	34	---
	χ-type phase	5.30	0.893	41	---
900 °C; GoF = 1.68, χ^2 = 2.75	FCC	48.00	0.362	49	0.52
	B2	33.70	0.290	53	0.37
	$Cr_{23}C_6$	10.00	1.066	36	---
	Cr_3Si	5.00	0.455	37	---
	χ-type phase	3.30	0.893	48	---
SPSed; GoF = 1.47, χ^2 = 2.15	FCC	47.00	0.362	42	0.21
	B2	30.00	0.290	43	0.18
	$Cr_{23}C_6$	15.00	1.066	24	---
	Cr_3Si	8.00	0.455	32	---

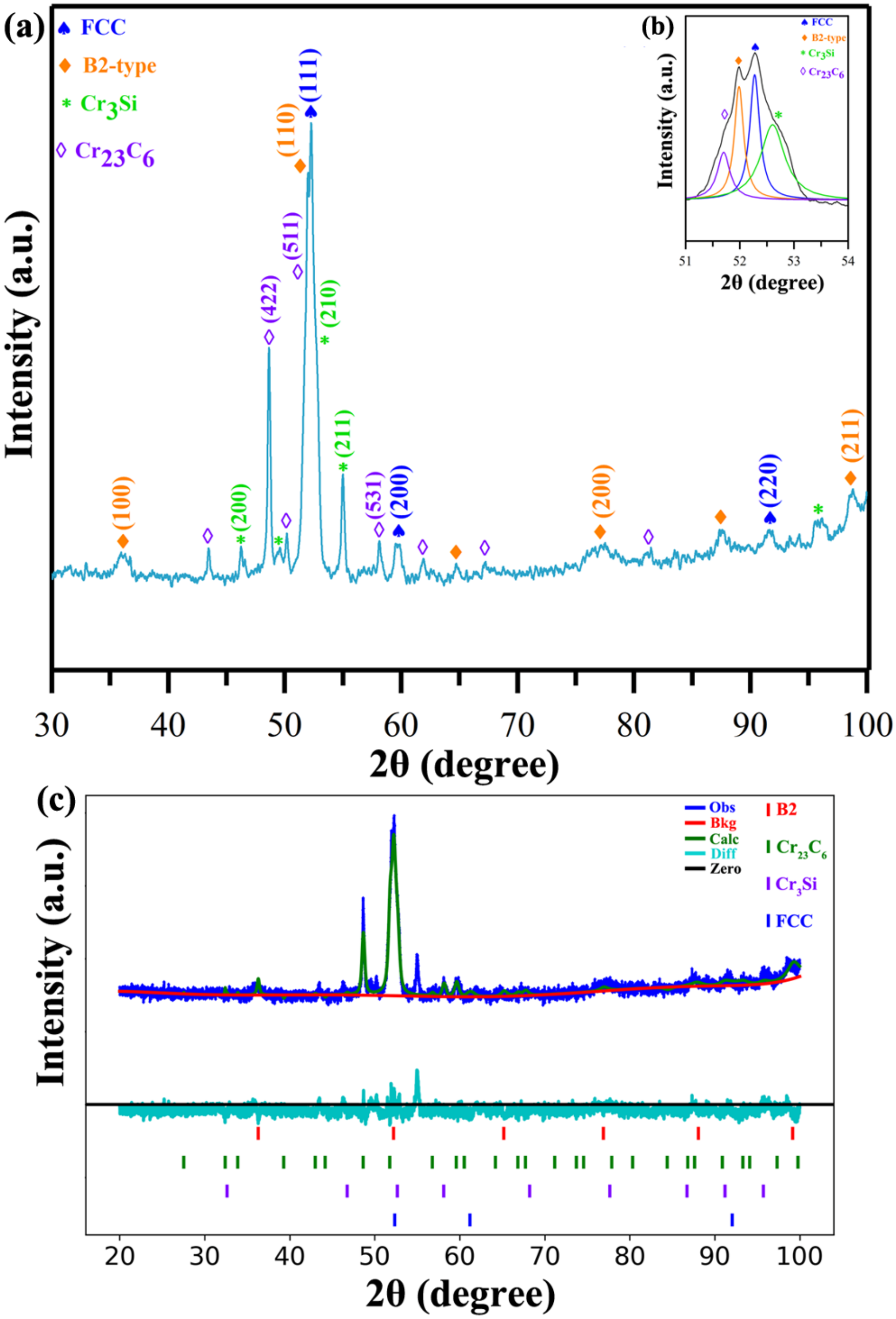

Figure 4.8: (a) XRD pattern of SPSed sample; (b) Deconvoluted image along the (111) plane; (c) Rietveld refinement of SPSed sample. The phases formed after the SPSed were FCC as the major phase, B2 as minor phase along with the intermetallics $Cr_{23}C_6$ and Cr_3Si type.

Figure 4.9(a and b) show the SEM (Back Scattered Electron) micrographs of the sintered sample of non-equiatomic FeMnNiCrAlSiC high entropy steel at different magnifications. In the magnified image (Figure 4.9(a)) it is seen that the surface morphology of a sintered sample of non-equiatomic FeMnNiCrAlSiC high entropy steel contains two different types of areas, both are irregular bulk types but the one in light shade region (marked as one) and other is in the dark shaded region (marked as two). It is also observed from Figure 4.9(a) that the nanoprecipitates of spherical shape with two different shades of light and dark grey are visible. Figure 4.9(c) shows the full area EDS spectrum, which is marked in Figure 4.9(a). The Energy Dispersive Spectra (SEM-EDS) at different locations are listed in Table 4.4. The point EDS confirms that the light grey region corresponds to ordered BCC, which is rich in Fe, Ni, and Al. The dark grey region is related to the FCC phase, which is rich in Fe, Cr, and Mn. The light spherical precipitates may be related to $Cr_{23}C_6$ type carbide and black precipitates are related to the Cr_3Si silicide. The elemental mapping of the SPSed sample of non-equiatomic FeMnNiCrAlSiC high entropy steel is shown in Figure 4.10. The elemental mapping shows that certain region is rich in Fe, Ni, and Al, which is marked in a blue unsymmetrical line in Al (Figure 4.10). The certain region is rich in Fe, Mn, and Cr, which is marked in a white unsymmetrical line in Mn and Cr (Figure 4.10). The elements of non-equiatomic alloys are distributed uniformly and show chemical homogeneity as confirmed by SEM-EDS. The dual-phase structure is also confirmed by the point EDS and elemental mapping of the SPSed sample of the HES.

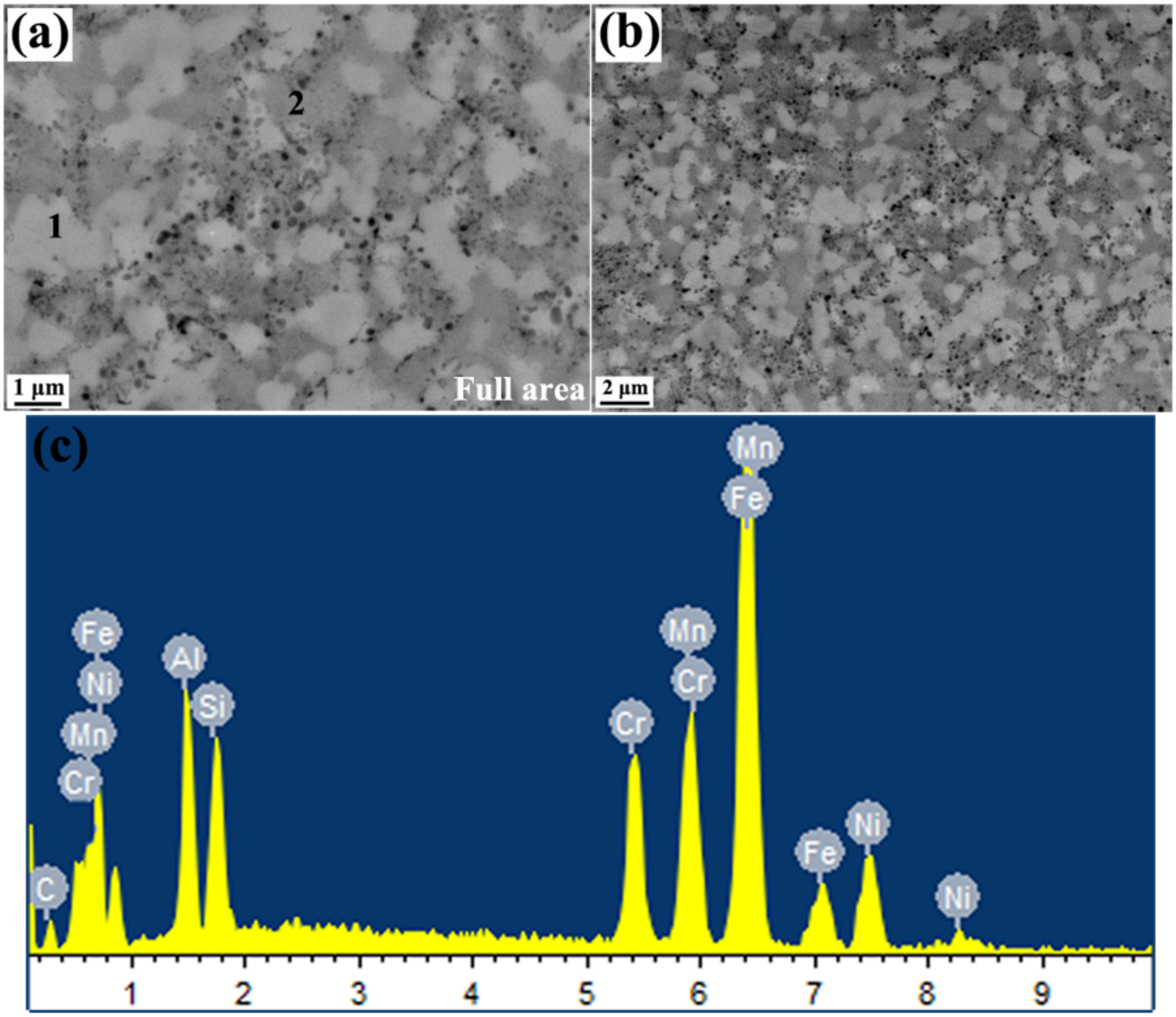

Figure 4.9: (a) and (b) SEM (BSE) image of the SPSed sample of the high entropy steel at different magnifications; (c) Full area EDS analysis of the marked area (in (a)). The different contrast i.e., light grey (1), dark grey (2) with light and dark grey spherical precipitates are clearly visible in SEM images.

Table 4.4: Elemental composition of SPSed sample of the HES2 at full area and point EDS.

Elemental composition (at%)							
Sample condition	**Scan area**	**Fe**	**Mn**	**Ni**	**Cr**	**Si**	**Al**
SPSed sample	**Full area**	41.60	13.50	11.00	9.30	9.10	14.40
	Spot 1	29.00	3.30	32.10	1.50	2.10	32.00
	Spot 2	47.16	20.82	5.23	16.34	3.24	8.21

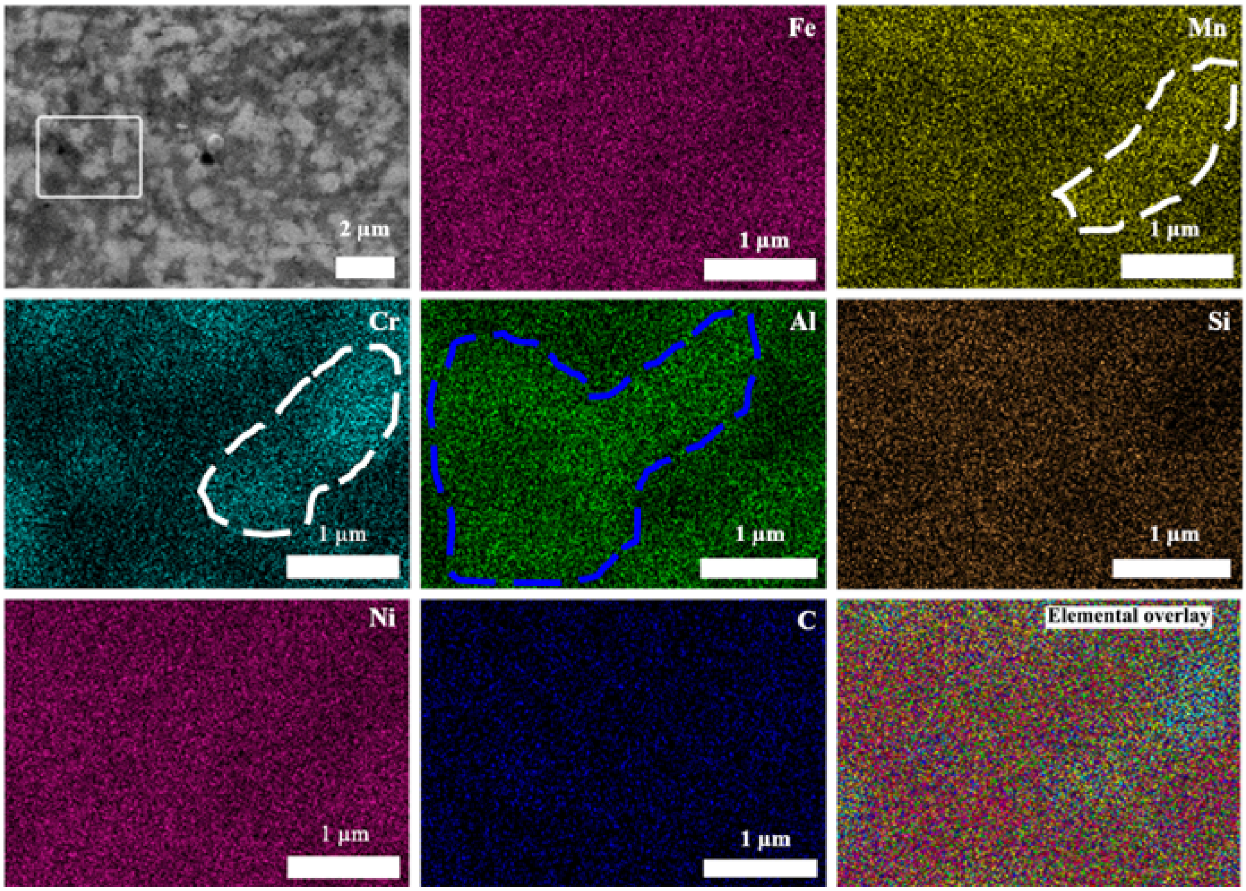

Figure 4.10: Elemental distribution and elemental overlay of the SPSed sample. Mapping shows the uniform distribution of the individual elements.

4.5 Physical and mechanical properties of the SPSed sample

The relative density was found to be ~99.4 % for the SPSed sample of non-equiatomic FeMnNiCrAlSiC high entropy steel, which was calculated as experimental density divided by theoretical density. The experimental density of the spark plasma sintered sample was measured using the Archimedes principal method, and its value was found to be 6.39 g/cc. The theoretical density of the alloy was found to be 6.43 g/cc, and it was calculated using the rule of mixtures. The sample seemed to be sound and no visible porosity was seen during SEM investigations. The experimental density measurement test was done for six times to calculate the average experimental density.

Figure 4.11(a) illustrates the response of the load vs indentation depth of the high entropy steel at an applied peak load of 5000 mN with loading rates of 1000 mN/s. It yielded a microhardness value of 7.4 ± 0.3 GPa and an elastic modulus of 189 ± 3 GPa, which is determined using the Oliver-Pharr analysis. The behaviour of the indentation curve illustrates the limited plasticity in this SPSed sample. Figure 4.11(b) depicts the optical micrograph of the indent at the maximum applied load on the surface of the SPSed sample, which depicts the no crack formation at 5000 mN load. The engineering stress-strain curves of the non-equiatomic FeMnNiCrAlSiC high entropy steel in the SPSed condition is displayed in Figure 4.11(c). The respective compressive properties, such as ultimate strength and compression to fracture are 1900 ± 100 MPa and 6.2 %, respectively. The physical and mechanical properties of the SPSed pellet are depicted in the form of a radar diagram, as shown in Figure 4.11(d). The radar diagram explicitly shows the relative density, microhardness, elastic modulus, compressive strength, and strain of the SPSed sample of high entropy steel.

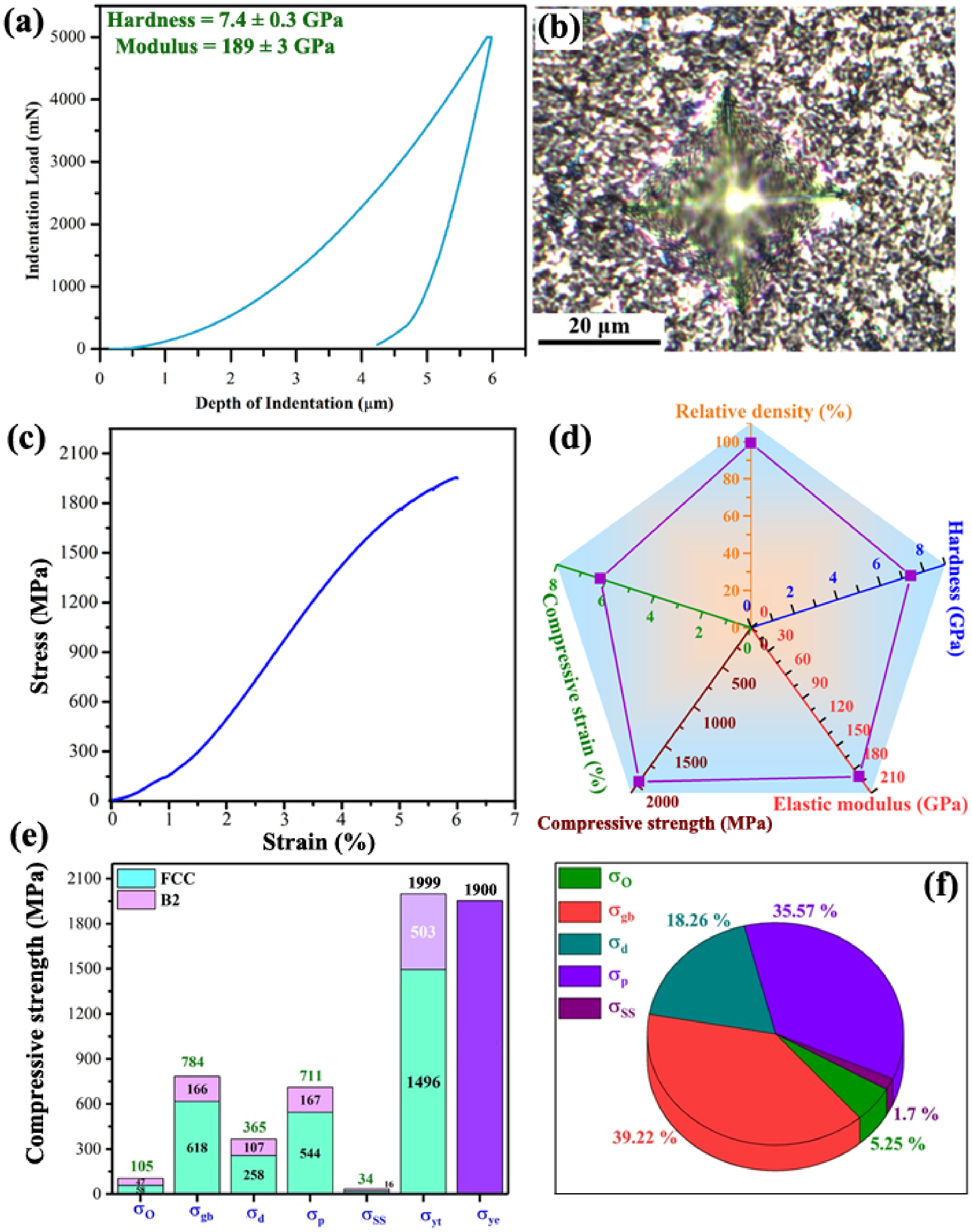

Figure 4.11: (a) Depth of penetration Vs Indentation load; (b) Optical micrograph of the indentation spot; (c) Compressive stress and strain curve; (d) The radar diagram manifests the physical and mechanical properties of the SPSed sample; (e) The values of the various strengthening mechanism and experimental yield strength (Bar plot); (f) The pie chart for the percentage's contribution of the various strengthening mechanism.

The fractured image of the SPSed sample at different magnifications is displayed in Figure 4.12(a and b). To understand the deformation behaviour of the fractured sample, SEM was done in secondary electron mode. The different types of fractured surface morphologies can be ascertained for non-equiatomic high entropy steel (Figure 4.12). The brittle quasi-cleavage fracture is evident in the fracture surfaces, which implicit that alloy is brittle. The crack is evident from the fractured surface, which might be due to the formation of hard intermetallic precipitates i.e., $Cr_{23}C_6$ carbide and Cr_3Si silicide after the spark plasma sintering. This is the reason behind the high strength with low ductility in the alloy.

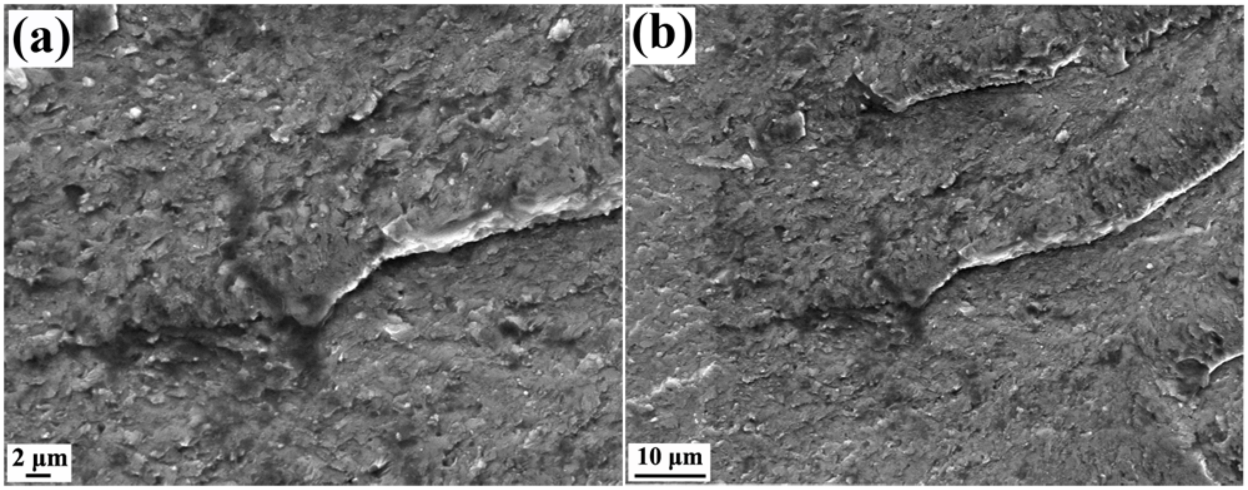

Figure 4.12: (a and b) SEM micrograph of the fractured sample at different magnifications after the compression test.

4.6 Surface properties of the SPSed sample

4.6.1 Wear study of the SPSed sample

Figure 4.13(a) displays the coefficient of friction curve with respect to time at ambient temperature under dry conditions. The reciprocating sliding wear test was done to study the tribological behaviour and mechanism in detail at different load conditions of 5 N, 10 N, and 20 N for the SPSed sample. The CoF values were evaluated to be 0.13 ± 0.02, 0.57 ± 0.05, and 0.83

± 0.03 at the load conditions of 20 N, 10 N, and 5 N, respectively, the increase in CoF with the normal load condition was evident from the Figure 4.13(a). This type of behaviour is also observed in the HEAs [236].

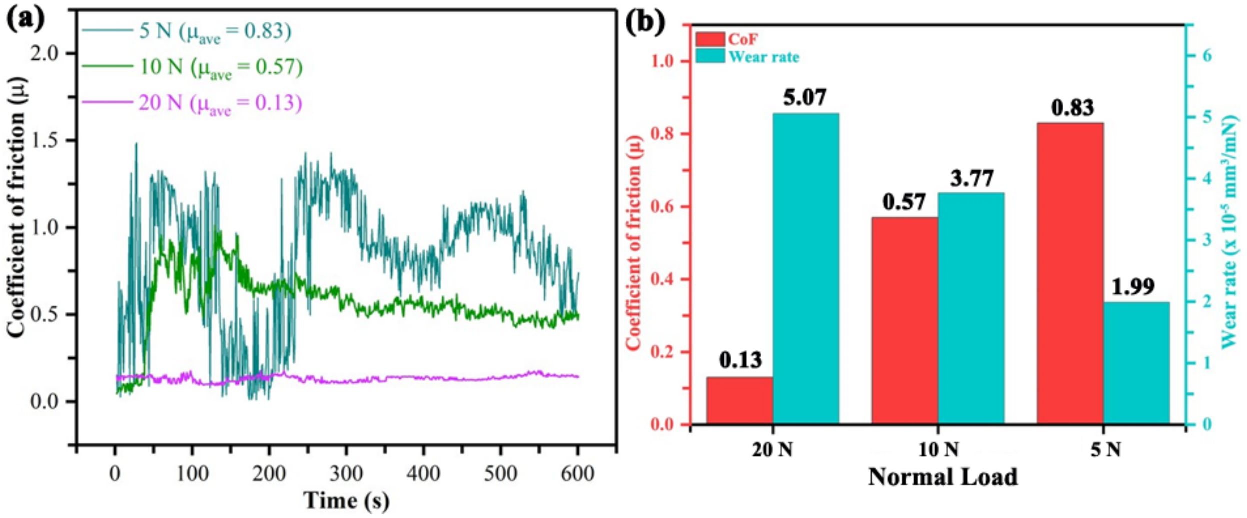

Figure 4.13: (a) Coefficient of friction vs time at different load conditions of the SPSed sample; (b) The values of the average CoF and specific wear rate at different load condition.

The CoF curves display the sawtooth behaviour with time, but under the 5 N load, they show the fluctuation kind of behaviour. The CoF increases in the early stages due to the slight deformation of surface roughness in the wear track, sticking of the abrasive tool onto the wear track, and fastening of the pin behind the roughness of the particles separated from the surface in those areas. However, as time increases the wear debris is removed, which leads to the elimination of surface heterogeneities resulting in the CoF eventually reaching to the steady state conditions. Sudden rise and fall in the CoF curves under 5 N load are due to the accumulation and segregation of wear debris on the surface. The variation in the CoF and specific wear rate of the SPSed sample at the load condition of 5 N, 10 N, and 20 N, as displayed in Figure 4.13(b), ascertained that the CoF decreases and specific wear rate increases with applied load.

To better understand the friction and wear behaviour of the alloy, a detailed study on the worn surface was done using the SEM. Figure 4.14(a, b, and c) displays the SEM image under the load condition of 5 N, 10 N, and 20 N, respectively at different magnifications. It is evident in the SEM images that the parallel shallow grooves grow along the sliding wear track, which developed due to the ploughing of micro-asperities between two friction surfaces with one hard counter (Al_2O_3). This kind of wear mechanism is due to abrasive and delamination. The wear debris is not observed at higher load conditions. The various features on the worn surfaces are marked by the black

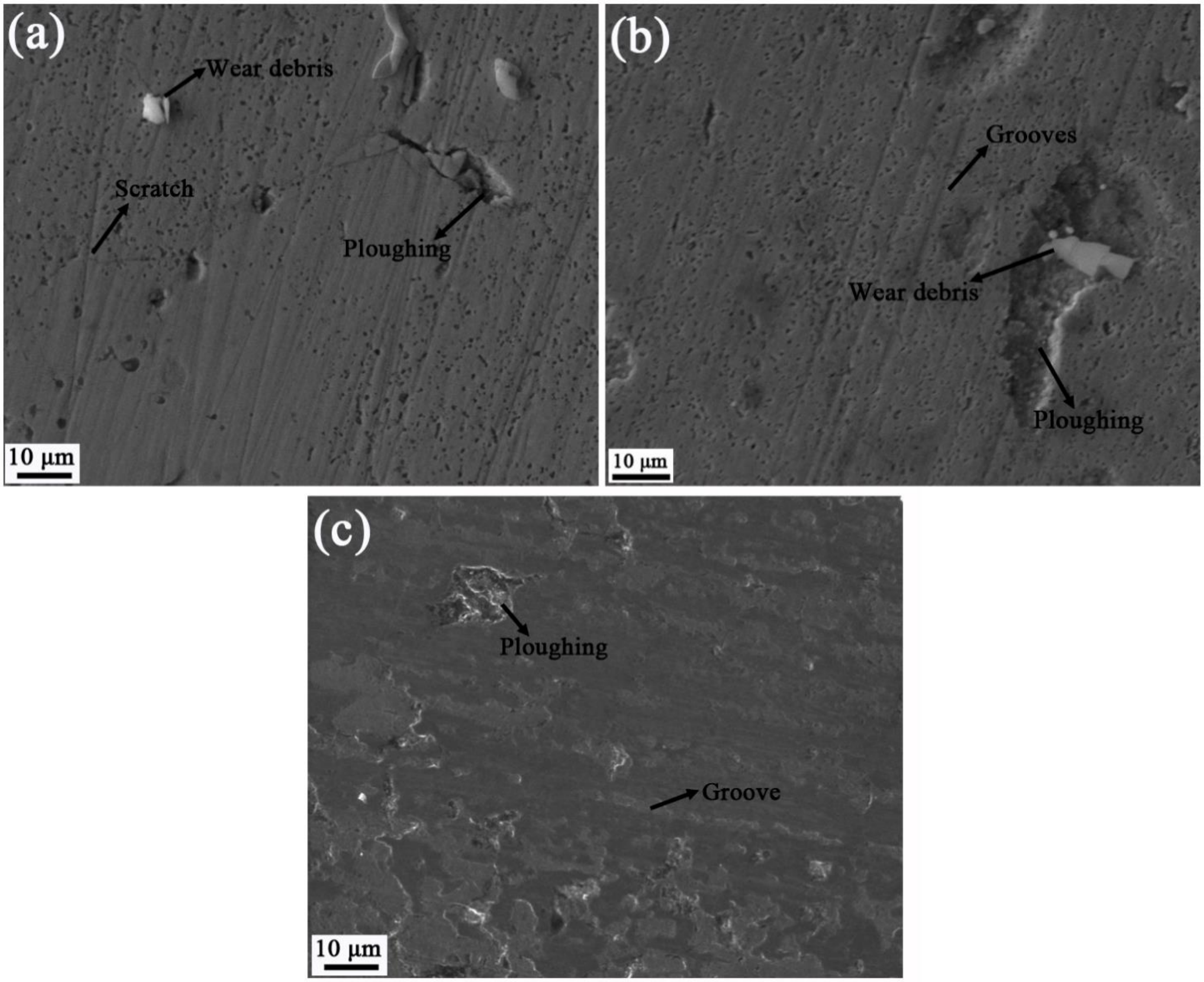

Figure 4.14: SEM (SE) micrographs of the worn surface at different magnifications at: (a) 5 N; (b) 10 N; (c) 20 N. These worn surfaces at different load condition shows the scratches, ploughing and wear debris features.

colour, as shown in Figure 4.14(a, b, and c). The fluctuations in the CoF curve at 5 N load conditions are also confirmed by the worn surfaces (Figure 4.14(a)), as the accumulation of wear debris is observed. This kind of behaviour in the wear mechanism is reported in main HEAs [236].

4.6.2 In-vitro biocompatibility analysis of SPSed sample

To investigate the cell viability of the high entropy steel and control (316L) were exposed to MG-63. Figure 4.15 illustrates the morphology and viability of MG-63 cells on the HES2 SPSed sample after 3, 5, and 7 days of seeding. The cell morphologies are perceived to be similar among control and SPSed samples (Figure 4.15). MTT results show that the initial viability at 3 and 5 days of cells in SPSed samples is slightly higher than the control sample. The cell viability of the alloy increases with the incubation period. However, for the incubation period of 7 days, the mean optical density ($p \leq 0.05$) of the non-equiatomic HES was significantly higher as compared to the control. The mean optical density ($p \leq 0.05$) of the high entropy steel is highest at 7 days as compared to 3 and 5 days with the control. Overall, the in-vitro study depicts that the SPSed samples preserve the morphology of MG-63 cells. The mean optical density was calculated using the equation no. 2.6. The FeMnNiCrAlSiC high entropy steel showed better biocompatibility as compared to 316L (major alloying elements are Cr, Ni, and Mo) due to the presence of Al, Mn, and Si, which has increased the biocompatibility of pure iron [263]. The reason for better biocompatibility of this alloy systems is presence of Mn and Si, which is present in very less amount in 316L. Mn helps to enhance the biocompatibility in metallic alloy systems, as Mn is an essential trace element that plays a primary role in the activation of multiple enzyme systems, such as hydrolases, kinases and decarboxylases [264–267]. The Si is well known alloying element used in biometallic alloys for various biomedical applications [268, 269]. Other than that Al and Cr is also to some extent helps for better biocompatibility in metallic alloy systems [270 ,271].

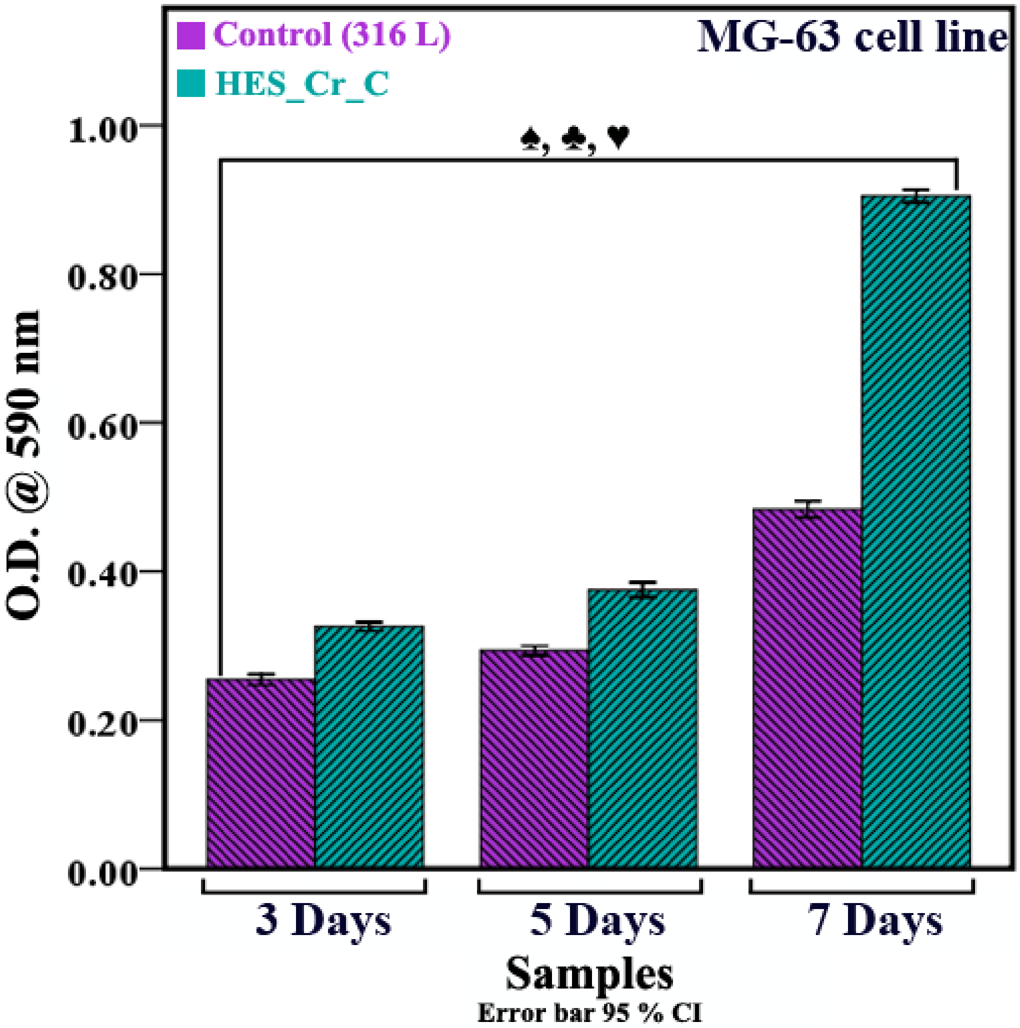

Figure 4.15: Concentration-dependent quantitative analysis (MTT assays) of MG-63 on control and SPSed sample after 3, 5, and 7 days. The symbol (♠) represents the statistically differences in the optical density (O.D.) among the SPSed sample with the control sample treated for 3, 5, and 7 days. The symbol (♣) represents the statistically differences in the O.D. among all the sample, treated for 5 days with respect to sample treated for 7 days. The symbol (♥) represents the statistically differences in the O.D. among all the sample treated for 7 days.

In TiMoNbTaW RHEA effect of Cr on in-vitro biocompatibility studies was carried out and it was found that the alloy showed the excellent cytocompatibility against MC3T3-E1 cells by increasing Cr due to the formation of Cr_2O_3, which contributes to enhance the cell viability [272]. So, due to the presence of Cr, Al, Mn and Si, elements in high entropy steel increases the biocompatibility, as the effect of these elements in the conventional alloy systems have already been reported [261, 262, 273].

4.7 Discussion

The phase evolution of non-equiatomic FeMnNiCrAlSiC high entropy steel during mechanical alloying is discussed on the basis of thermodynamics parameters. For the phase prediction of high entropy alloys, several parameters are proposed. It is known that the high configurational entropy of HEAs is not the only factor to dominate the formation of phases in HEAs systems. Lower diffusivity (kinetics) also helps to form a solid solution. Some useful criteria for phase formation for high entropy alloys are high mixing enthalpy (ΔH_{mix}), configurational entropy (ΔS_{conf}), and element radii mismatch (δ), and the detailed calculations are given in section 1.5. According to the findings, disordered solid solution forms when $-15 \leq \Delta H_{mix} \leq 5$ kJ/mol, $\Delta S_{conf} \geq 13.38$ J/mol-K, and $\delta \leq 6.6$ %. Further investigation on two more parameters i.e., Ω and valence electron concentration i.e., (VEC) were included to rationalize the formation of a solid solution in HEAs. For the formation of a single-phase HEA solid solution, the parameter should be within the ranges of $\Omega \geq 1$ and $\delta \leq 6.6$ %. These predictions support various previous HEA compositions for solid solution phase formation. All the parameters calculated for the non-equiatomic high entropy steel composition of present work is shown in Table 4.5, the calculated parameters are within the range of a single BCC phase and it forms BCC phase after 40 hours of MA. The heat of mixing values of different binary alloys is shown in Figure 4.16. Although the value of Ω is ~ 4, which is in the range, the value of δ is outside the limit as shown in Table 4.5. Therefore, in the present investigation, multi-solid solution phases are present in the high entropy steel that was observed after SPS. The formation of intermetallic after SPS might be the case of the heat of mixing values of different binary alloys. The chance for the formation of the intermetallic compound was due to

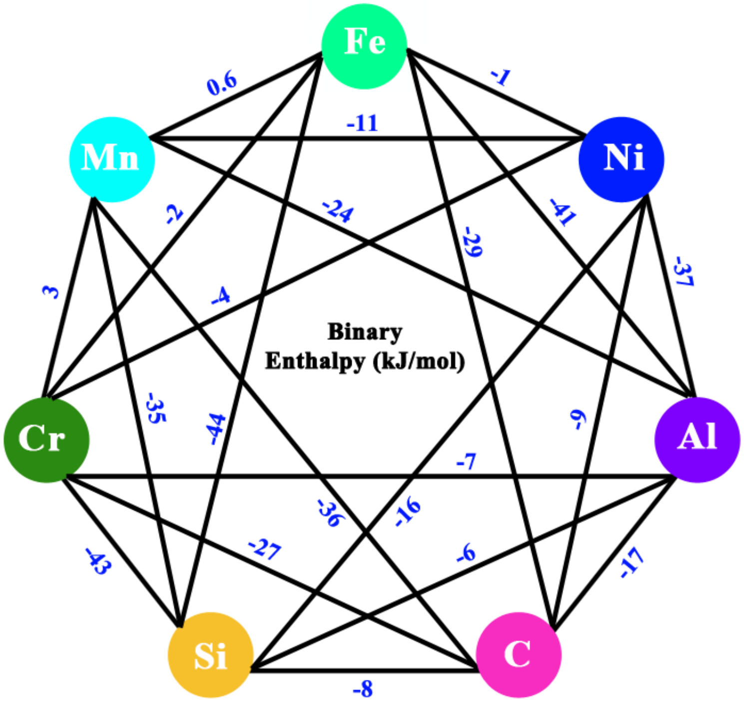

Figure 4.16: Binary enthalpy (kJ/mol) of all the binary pairs in the non-equiatomic FeMnNiCrAlSiC HES.

the enthalpy of mixing being highly negative in some binary pairs of the present alloy system. The enthalpy of binary alloys Cr-Si and Cr-C is highly negative, and another reason might be that Cr has very high electron affinity to form an intermetallics compound with Si and C.

The decrease in peak intensity and increase in broadening was observed during the milling, this is due to decrease in crystallite size and increase in lattice strain with milling time. The experimental results of non-equiatomic FeMnNiCrAlSiC high entropy steel clearly show the dual-phase structure consisting of BCC phase (close to Fe) and χ-type phase structure after the 40 hours of mechanical milling. The phase evolution of non-equiatomic high entropy steel is also dependent on the physical parameters of individual elements, and its value is mentioned in Table 2.3. The selection of the host lattice concept in HEAs is due to the melting point of individual elements, as elements having a higher melting point, have higher bond strength and stability compared to elements with low melting point [140]. The non-equiatomic high entropy steel phase evolution also depends upon the above parameters. The melting point of Fe and Cr is the highest among all the other elements used. So, Fe acts as the host lattice for the BCC phase as evident from the lattice parameter.

Table 4.5: Calculated thermodynamic parameters of the HES2.

ΔH_{mix} (kJ/mol)	**δ (%)**	**ΔS_{conf} (J/mol-K)**	**Ω**	**VEC**
-5.4	7.5	13.44	4	6.67

Figure 4.17(a) illustrates the calculated equilibrium phase fraction as a function of temperature ranging from 50 °C to 1300 °C of non-equiatomic FeMnNiCrAlSiC high entropy steel using the steel database TCFE8. According to the Thermocalc calculation, the equilibrium microstructure of this HES consists of the dual-phase structure i.e., BCC and FCC structure at high temperature, from the solidus at around 1220 °C down to about 50 °C and at 1220 °C to 1050 °C, respectively. At lower temperature the intermetallic Cr_3Si and $M_{23}C_6$ is also stable from 750 °C to 50 °C and 1070 °C to 150 °C, respectively. At lower temperature BCC_A2#2 from 380 °C to 50 °C is stable. Figure 4.17(b-f), shows the equilibrium composition of the various phase i.e., two BCC, FCC, $M_{23}C_6$, and Cr_3Si, respectively, and its relatively constant composition over the temperature range was display. The BCC_A2#2 is rich in Fe and also have other elements in less quantity. Fe, Mn, and Si rich is corresponding to BCC_A2 phase as shown in Figure 4.17(b). The FCC phase contains comparable amounts of Fe and Mn, with presence of Cr, Ni, Al, Si, and C according to the calculations (Figure 4.17(c)). Figure 4.17(e and f) shows the stability of the Cr, Mn and C, and Cr and Si, respectively with temperature, and it shows the stable compositional variation in both

the intermetallic compounds. The $M_{23}C_6$ intermetallic contains comparable amounts of Cr, Mn, Fe and C according to the calculations but changes in temperature were ascertained (Figure 4.17(e)).

The present equilibrium phase fraction from CALPHAD calculation does not match well with the experimental findings of this HES. The phase shows after the milling are two BCC structures, and this was well correlated with the CALPHAD phase predictions. However, at room temperature the intermetallic compounds i.e., silicide and carbide were also predicted, but this kind of compound formation was not observed after the milling. The phases formed after the SPSed sample are FCC, B2 with Cr_3Si and $Cr_{23}C_6$ intermetallic compound, this was somewhat close to the phase predictions. But there is some disparity with the phase predictions at elevated temperature, the phase fraction of FCC is less in phase predictions while in experiment it is more, and it showed the BCC phase prediction (as major phase) but in experiment it is B2-type phase (as secondary phase). This disagreement could be a consequence of the description being limited to extrapolation of the ThermoCalc database and thus failure to predict phases that would be stable in a multicomponent system.

To substantiate the overall strength of the high entropy steel SPSed sample is correlated with various strengthening mechanisms. Various contributions calculated here are frictional (σ_o), grain size (σ_{gb}), dislocation (σ_d), precipitation (σ_p), and solid solution (σ_{ss}) strengthening. The experimental yield stress of the SPSed sample was found to be 1900 ± 100 MPa. The theoretical yield stress can be taken from equation no. 1.9. The values of the frictional stress are taken as 95.4 MPa and 120 MPa for FCC and B2-type [225], respectively. The Hall-Petch relation was used to calculate the contribution of grain size strengthening, and it is taken from equation no. 1.13. The term used in this equation is, K_o = material constant, and its value was considered as 823 MPa/ $\mu m^{1/2}$ and 155 MPa/$\mu m^{1/2}$ for FCC and B2-type [225], respectively, and d is the grain size. The

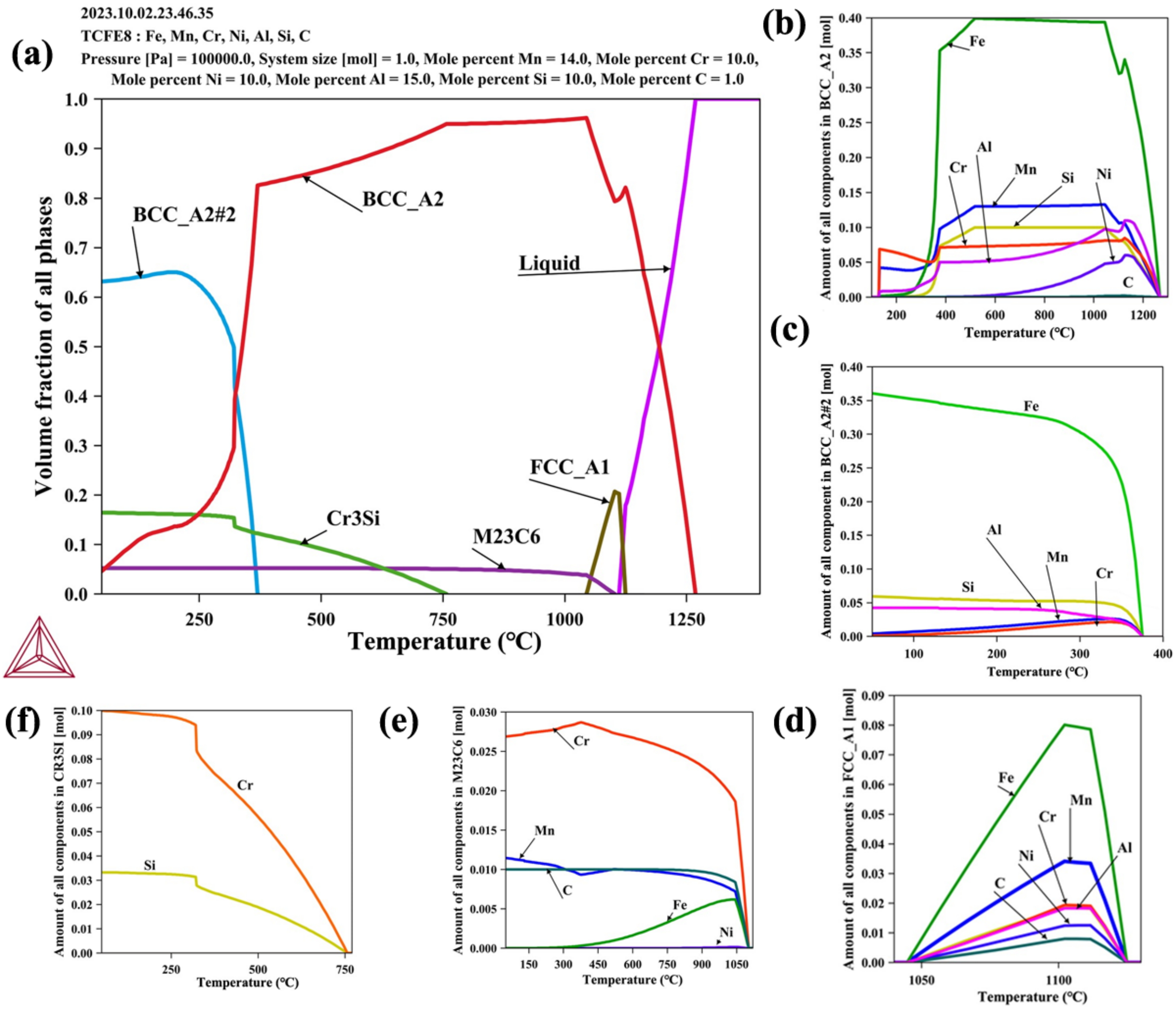

Figure 4.17: (a) Property diagram of the non-equiatomic FeMnNiCrAlSiC high entropy steel; (b-f) The elemental composition in all the phases and their stability with respect to temperature.

value of the grain size for FCC and B2-type was found to be 0.660 μm and 0.133 μm, respectively. The value for grain boundary strengthening was found to be 1013 MPa and 425 MPa for FCC and B2-type, respectively.

The effect of the carbide, silicide, and the B2-type precipitate on the FCC phase was calculated using equation no. 1.14 and 1.15. The values of the various term in the equation for the present alloys are, M = 3.06 and 2.73 for FCC and B2-type [225], respectively, G = shear modulus, evaluated by the rule of mixture, and its value is taken as 70.9 GPa, υ = Poisson's ratio (0.3), b = Burger vector, and its detail calculation of the respective phases are given in subsection 2.3.1, a = lattice parameter, and value is listed in Table 4.3, and r = mean radius of the precipitates (102 nm for Cr_3Si-type, 80 nm for $Cr_{23}C_6$). The value of the dispersion strengthening for the FCC phase was found to be 313 MPa, 154 MPa, and 425 MPa for carbide, silicide, and B2-type, respectively, and for the B2-type phase was found to be 293 MPa and 135 MPa for carbide and silicide, respectively.

The contribution of the dislocation strengthening was calculated using the equation no. 1.12, where the values of various terms are $\alpha = 0.2$ for FCC and B2-type [225], respectively, b = Burger vector, and ρ_{dd} = dislocation density, and the values are listed in Table 4.3. The value of the dislocation strengthening was attained to be 424 MPa and 344 MPa for FCC and B2-type, respectively.

The solid solution strengthening was calculated using equation no. 1.10 and 1.11. The values of the various terms are, c = atomic (%) of the solute element (Al), and its values are listed in Table 4.4. The solid solution strengthening value was found to be 29 MPa and 40 MPa for FCC and B2-type, respectively.

To calculate the theoretical strengthening mechanism in the present alloy, some assumptions were made, one of which was that the total phase fraction of the FCC and B2-type was taken as 100%. However, the phase fraction of FCC and B2-type in the SPSed sample was determined as 47.0 % and 30.0 %, respectively. Therefore, for the strengthening mechanism calculation, the phase fraction was taken as 61.0 % and 39.0 % for FCC and B2-type phases, respectively. Figure 4.11(e) displays the values of the individual strengthening mechanism of the present alloy. The distribution of the various strengthening mechanisms is shown in the bar chart, as illustrated in Figure 4.11(f). It is evident from the Figure 4.11(f), that the grain boundary and precipitation strengthening are major strengthening mechanisms. There is some disparity in the experimental and theoretical strength of the present alloy, which is in tolerable range.

In the present investigation, the high hardness of non-equiatomic FeMnNiCrAlSiC high entropy steel is due to the formation of the B2-type phase, Cr_3Si and $Cr_{23}C_6$ intermetallic compound, and the nanocrystalline structure. The fine particles of Cr_3Si and $Cr_{23}C_6$ intermetallic compounds are irregular in shape and evenly disturbed in the matrix. Jin et al. [274] showed the phase transformation in $FeCoCrNiAl_{0.5}Si_x$ alloy ($x = 0.0 – 2.0$, at. %) from a mixture of BCC and FCC solid solution to a mixture of BCC solid solution and Cr_3Si precipitates as Si content increases. The BCC phase volume increases with the addition of Si and so is the hardness. Chen et al. [173] and Baker et al. [45] prepared HEAs by VAM, which showed good mechanical properties due to the formation of a dual-phase structure mainly consisting of FCC/BCC with some precipitates.

Wear depends on both the strength and ductility of the material. The Archard equation is only related to two types of wear i.e., adhesive, and abrasive wear. It is universally known that the wear rate increases with the applied load. Thus, at higher applied load (20 N) the wear loss is nominally high as compared to that of the lower load condition. This is due to the fact that the worn surface at 20 N load shows more ploughing in the wear track as compared to that of 5 N load condition, as shown in Figure 4.14 (a, and c). This kind of wear behaviour is also observed in the other metallic alloys [236, 275]. In the present work of non-equiatomic high entropy SPSed steel sample, the phases formed are FCC+B2 and it is supposed to provide a combination of strength and ductility. Hence the wear rate is low, and also it shows nominal change in wear rate with varying load condition. The wear resistance of the present alloy is better than the known dual-phase steel, conventional steel, and HEAs [169, 252, 253, 276].

4.8 Conclusions

The following conclusions is drawn from the present chapter as:

1. In the present study, non-equiatomic FeMnNiCrAlSiC high entropy steel is successfully synthesized using mechanical alloying followed by spark plasma sintering, and it was formed the metastable dual-phase consisting of BCC and χ-type phase solid solution after 40 h of milling.
2. This alloy showed the good thermal stability up to 400 °C, afterwards at higher temperature it formed the FCC solid solution, $Cr_{23}C_6$ and Cr_3Si.
3. High entropy steel with good density and fine microstructures has been effectively processed by SPS, which leads to the formation of the dual-phase structure consisting of FCC/B2 phases along with Cr_3Si and $Cr_{23}C_6$ intermetallics.
4. The mechanical properties i.e., microhardness, elastic modulus, yield compressive strength, and ductility of the alloy are 7.4 ± 0.3 GPa, 189 ± 3 GPa, 1900 ± 100 MPa, and 6.5 %, respectively. The high strength of the alloy is due to grain boundary and precipitation strengthening.
5. The surface property i.e., tribology of the alloys is estimated, and its value (specific wear rate) was found in the range of $1.99 – 5.07 \times 10^{-5}$ mm^3/mN with the varying load condition. The abrasion and delamination kind of wear mechanism is the dominant mechanism in high entropy steel. This alloy has better biocompatibility as compared to 316L stainless steel in the MG-63 cell.

6. The semi-empirical thermodynamics parameters are not in the range of solid solution forming criteria of high entropy alloys, and it is also observed from the experimental findings that the empirical phase formation criteria are violated. The phase prediction using the CALPHAD modelling have some disparity with experimental findings, this difference is might be due to the available TCFE8 database which is not optimised for multicomponent systems.